Journal of Superconductivity and Novel Magnetism (2025) 38:229
https://doi.org/10.1007/s10948-025-07069-5

RESEARCH

Numerical and Theoretical Analyses of Losses in Armature Windings of Motors for Liquid Hydrogen Pumps

Kazuhiro Kajikawa[1] · Yuto Mametsuka[1] · Masahiro Furukakoi[1] · Taketsune Nakamura[2] · Akihiro Kikuchi[3] · Tomohito Miura[4]

Received: 2 September 2025 / Accepted: 15 October 2025 / Published online: 30 October 2025
© The Author(s) 2025

Abstract
In order to develop submerged pumps to transfer liquid hydrogen, high temperature superconducting (HTS) motors to drive them as one of key components are a promising candidate with low electromagnetic loss and large specific power density per unit mass. However, since armature windings wound using HTS wires have a couple of problems such as three-phase unbalanced currents and frequency limitations, HTS wires are used only for rotor windings of the motors and metallic cables have to be applied to their armature windings. Therefore, numerical analyses to evaluate loss properties in multi-strand metal twisted cables for armature windings of HTS motors cooled at liquid hydrogen temperature are carried out by means of a two-dimensional finite element method. On the basis of a clarified physical mechanism of losses generated in the windings arranged within a slot of armature iron core, the obtained numerical results are also reproduced with theoretical expressions of the Joule loss for an alternating transport current and the eddy-current loss for an externally applied AC magnetic field. The influences of losses on the frequency and number of strands in metal twisted cables are investigated quantitatively.

Keywords Armature winding · Eddy current loss · Joule loss · Finite element method · Theory

1 Introduction

Many governments around the world have officially pledged to achieve carbon neutrality by the middle of the 21st century, aiming to offset greenhouse gas emissions with equivalent absorption, thereby reducing net emissions to zero [1]. It has been expected to use hydrogen as one of key technologies to realize the carbon neutrality up to now. It is well known that the hydrogen does not exist alone in the earth but is included in water, organic compounds, etc.,

Kazuhiro Kajikawa, Yuto Mametsuka, Masahiro Furukakoi, Taketsune Nakamura, Akihiro Kikuchi, Tomohito Miura contributed equally to this work.

✉ Kazuhiro Kajikawa
kajikawa@rs.socu.ac.jp

Yuto Mametsuka
f124620@ed.socu.ac.jp

Masahiro Furukakoi
furukakoi@rs.socu.ac.jp

Taketsune Nakamura
nakamura.taketsune.2a@kyoto-u.ac.jp

Akihiro Kikuchi
KIKUCHI.Akihiro@nims.go.jp

Tomohito Miura
t-miura@torishima.co.jp

[1] Department of Electrical Engineering, Sanyo-Onoda City University, 1-1-1 Daigaku-Dori, 756-0884 Sanyo-Onoda, Yamaguchi, Japan

[2] Department of Electrical Engineering, Kyoto University, 1-30 Goryo-Ohara, Nishikyo-ku, 615-8245 Kyoto, Kyoto, Japan

[3] National Institute for Materials Science, 1-2-1 Sengen, 305-0047 Tsukuba, Ibaraki, Japan

[4] Torishima Pump Mfg. Co., Ltd., 1-1-8 Miyada-cho, 569-8660 Takatsuki, Osaka, Japan

so that a series of supply chains for the hydrogen to be produced, stored, transported and utilized has to be established safely and stably. Although the hydrogen itself has a poor volume density, the liquefaction is one of realistic solutions for the effective use of hydrogen, especially during its storage and transportation. The application of high temperature superconductors (HTSs) with the liquid hydrogen such as a power cable [2], generator [3], superconducting magnetic energy storage (SMES) [4], active magnetic refrigeration (AMR) [5], magnets [6–8], level sensors [9–11], and so on, has been fabricated and tested so far. The submerged pumps for liquid hydrogen driven by HTS motors, which will be necessary as one of infrastructures in future hydrogen society, have also been evaluated experimentally [12–14], where MgB_2 wires have been applied to squirrel-cage windings in the rotor.

In order to realize the submerged pumps for liquid hydrogen, it is important to reduce losses in armature windings of the drive motor cooled at cryogenic temperature, which have three-phase alternating currents to generate a rotating magnetic field inside and then rotate the rotor. Generally, two types of conductors are considered for motor armature windings: HTS wires and low-resistivity metallic cables. Fully superconducting motors, where HTS materials are applied to both rotors and stators, have been fabricated and tested up to now [14–18]. When HTS wires are used for the armature windings energized with a widely used voltage drive inverter, however, it has been found that the risk of burnout of them might arise due to unbalanced three-phase currents and therefore the HTS wires could not be applied to them [19]. It has also been reported that, at frequencies of several hundred hertz, the weights and losses in the armature windings of motors cooled to liquid hydrogen temperature using fine multi-strand metallic cables with high residual resistivity ratios (RRRs) are lower than those estimated with HTS wires [20]. It is well known that the electrical resistivity of metals decreases with temperature, and that the Joule loss for an alternating transport current also decreases with resistivity. On the other hand, the eddy-current loss for an externally applied AC magnetic field increases with decreasing the resistivity and can be suppressed by using thin wires, which also leads to avoid the skin effect at cryogenic temperature. As a result, it has recently begun evaluating losses in multi-strand metal cables under cryogenic conditions. [20–25].

In this study, the numerical analyses to evaluate loss properties in multi-strand metal twisted cables arranged within iron core slots are carried out by means of a two-dimensional finite element method. The obtained numerical results are also reproduced with another numerical model and derived theoretical expressions. The influences of losses on frequency and number of strands in metal twisted cables at liquid hydrogen temperature are investigated quantitatively.

2 Theoretical Expression of Joule Loss in Round Wire

Let us derive a theoretical expression of Joule loss in a round wire made of a normal metal with a radius r_s and an infinite length in the z-direction. Figure 1 shows the local current density J_z and magnetic field H_θ inside the round wire, to which the transport current $I_t = I_e\, e^{j\omega t}$ is applied, where I_e is the root mean square (RMS) value of transport current and $\omega\ (= 2\pi f)$ is the angular frequency with the frequency f. In this case, the current density J_z and magnetic field H_θ satisfy the modified Bessel differential equations,

$$\frac{\partial^2 J_z}{\partial u^2} + \frac{1}{u}\frac{\partial J_z}{\partial u} - J_z = 0, \tag{1}$$

$$\frac{\partial^2 H_\theta}{\partial u^2} + \frac{1}{u}\frac{\partial H_\theta}{\partial u} - \left(1 + \frac{1}{u^2}\right) H_\theta = 0, \tag{2}$$

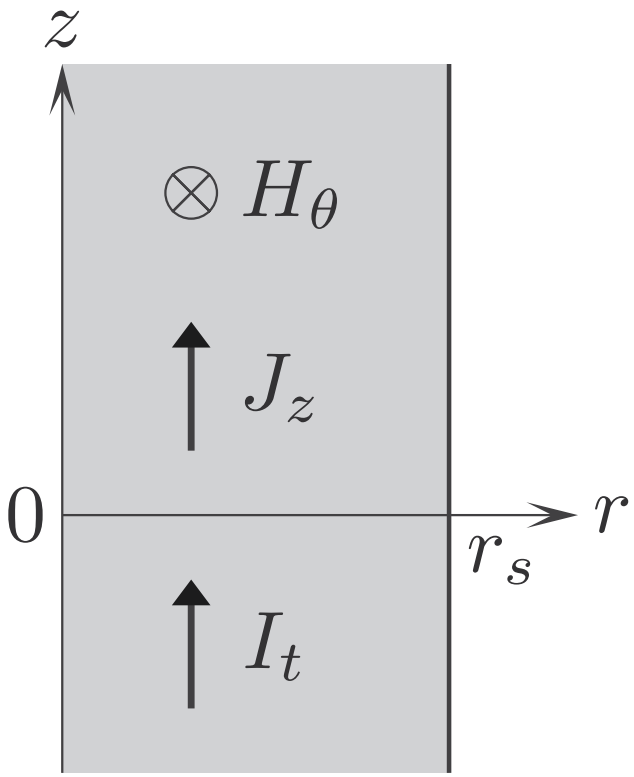

Fig. 1 Local current density J_z and magnetic field H_θ inside round wire made of normal metal with radius r_s and infinite length, to which transport current I_t is applied

obtained easily from Maxwell's equations, where the normalized variable u is given by $u = \alpha r$ with the parameter α represented by

$$\alpha = \sqrt{\frac{j\omega\mu_0}{\rho_s}} = \frac{1+j}{\lambda_s}, \tag{3}$$

where j is the imaginary unit and λ_s is the skin depth given by $\lambda_s = \sqrt{2\rho_s/(\omega\mu_0)}$ with the resistivity ρ_s.

The exact solutions for (1) and (2) can be expressed as [26]

$$J_z = c_1 I_0(u)\, e^{j\omega t}, \tag{4}$$

$$H_\theta = c_2 I_1(u)\, e^{j\omega t}, \tag{5}$$

by using the constants of integration, c_1 and c_2, having a relationship $c_1 = \alpha c_2$, and the modified Bessel function of the first kind, $I_n(u)$, which is simply represented by

$$I_n(u) = \frac{1}{\pi}\int_0^\pi e^{u\cos q}\cos nq\,\mathrm{d}q, \tag{6}$$

for an integer n, where q is the integral variable. The boundary condition is given by $H_\theta|_{r=r_s} = I_t/(2\pi r_s)$, so that the time-domain formulations of the transport current I_t, current density J_z, and magnetic field H_θ are ultimately obtained by transforming the corresponding phasor representations as

$$I_t(t) = \sqrt{2}\,\mathrm{Im}\left[I_e\, e^{j\omega t}\right] = \sqrt{2}\, I_e \sin\omega t, \tag{7}$$

$$\begin{aligned} J_z(r,t) = J_e \frac{r_s}{\lambda_s}\sqrt{\frac{G_1^2(r)+G_2^2(r)}{G_3^2(r_s)+G_4^2(r_s)}} \\ \times \sin\left[\omega t + \frac{\pi}{4} + \varphi(r) - \psi(r_s)\right], \end{aligned} \tag{8}$$

$$\begin{aligned} H_\theta(r,t) = H_m\sqrt{\frac{G_3^2(r)+G_4^2(r)}{G_3^2(r_s)+G_4^2(r_s)}} \\ \times \sin[\omega t + \psi(r) - \psi(r_s)], \end{aligned} \tag{9}$$

where $J_e = I_e/\left(\pi r_s^2\right)$ and $H_m = \sqrt{2}\, I_e/(2\pi r_s)$. The functions, G_1, G_2, G_3 and G_4, are expressed as

$$G_1(r) = \frac{1}{\pi}\int_0^\pi e^{\frac{r}{\lambda_s}\cos q}\cos\left(\frac{r}{\lambda_s}\cos q\right)\mathrm{d}q, \tag{10}$$

$$G_2(r) = \frac{1}{\pi}\int_0^\pi e^{\frac{r}{\lambda_s}\cos q}\sin\left(\frac{r}{\lambda_s}\cos q\right)\mathrm{d}q, \tag{11}$$

$$G_3(r) = \frac{1}{\pi}\int_0^\pi e^{\frac{r}{\lambda_s}\cos q}\cos\left(\frac{r}{\lambda_s}\cos q\right)\cos q\,\mathrm{d}q, \tag{12}$$

$$G_4(r) = \frac{1}{\pi}\int_0^\pi e^{\frac{r}{\lambda_s}\cos q}\sin\left(\frac{r}{\lambda_s}\cos q\right)\cos q\,\mathrm{d}q. \tag{13}$$

The functions, φ and ψ, are also given by

$$\varphi(r) = \arctan\frac{G_2(r)}{G_1(r)}, \tag{14}$$

$$\psi(r) = \arctan\frac{G_4(r)}{G_3(r)}. \tag{15}$$

By using (8), the local power dissipation p per unit volume can become

$$\begin{aligned} p(r) &= \frac{\omega}{2\pi}\int_0^{\frac{2\pi}{\omega}} \rho_s J_z^2(r,t)\,\mathrm{d}t \\ &= \frac{\rho_s J_e^2}{2}\frac{r_s^2}{\lambda_s^2}\frac{G_1^2(r)+G_2^2(r)}{G_3^2(r_s)+G_4^2(r_s)}. \end{aligned} \tag{16}$$

Therefore, the total power dissipation P_J per unit length can be obtained as

$$\begin{aligned} P_J = \int_0^{r_s} 2\pi r p(r)\,\mathrm{d}r = \frac{P_0}{G_3^2(r_s)+G_4^2(r_s)} \\ \times \int_0^{\frac{r_s}{\lambda_s}} \frac{r}{\lambda_s}\left[G_1^2(r)+G_2^2(r)\right]\mathrm{d}\left(\frac{r}{\lambda_s}\right), \end{aligned} \tag{17}$$

where P_0 is the power dissipation per unit length in the case where the current uniformly flows inside the round wire, which is given by $P_0 = \rho_s J_e^2 S_s$ with the cross-sectional area S_s $\left(= \pi r_s^2\right)$ of the round wire. The validity of (17) is confirmed in Section 4.

3 Numerical Calculations of Losses

Four kinds of metallic cables considered in this study are listed in Table 1. The number of strands, N_s, in twisted cables is 7, 19 or 37 as well as 1 for a single solid round wire. The diameter of the single wire is 0.812 mm, which corresponds to 20 American wire gauge (AWG), whereas the diameter $2r_s$ of strands in 7-, 19- and 37-strand cables are 0.255 mm, 0.143 mm and 0.101 mm, respectively, which correspond to 30, 35 and 38 AWG. Although the diameters of strands, $2r_s$, are different from each other, the outer diameters $2r_h$ in the multi-strand cables are identical to that for the single wire by adjusting the distances d between adjacent layers

Table 1 Specifications of metallic cables

Number of strands, N_s	1	7	19	37
Diameter of strand, $2r_s$	0.812 mm (20 AWG)	0.255 mm (30 AWG)	0.143 mm (35 AWG)	0.101 mm (38 AWG)
Distance between adjacent layers in cable, d	-	0.0235 mm	0.0243 mm	0.0175 mm
Outer diameter of cable, $2r_h$	0.812 mm (20 AWG)	0.812 mm (20 AWG)	0.812 mm (20 AWG)	0.812 mm (20 AWG)
Volume fraction of strands, ϕ	100%	69.0%	58.9%	57.2%
Resistivity of strand, ρ_s [27]	0.167 nΩ·m	0.167 nΩ·m	0.167 nΩ·m	0.167 nΩ·m
Characteristic frequency, f_s	257 Hz	2.60 kHz	8.27 kHz	16.6 kHz
RMS value of applied current, I_e	20 A	20 A	20 A	20 A

in the twisted cables. In this case, the volume fractions of strands, ϕ $\left(= N_s r_s^2 / r_h^2\right)$, vary from 100% in the single wire to 57.2% in the 37-stand cable, and decrease monotonically with increasing the number of strands. The resistivity of copper, 0.167 nΩ·m, at 20 K and 0 T with RRR of 100 is used [27], and no magnetic-field dependence of resistivity is considered here [28]. The characteristic frequencies f_s, at which the skin depth becomes equal to the radius r_s of strand, are 257 Hz for the single wire, and 2.60, 8.27 and 16.6 kHz for the 7-, 19- and 37-strand cables, respectively. The RMS value of transport current applied to the cable, I_e, is fixed at 20 A.

Figure 2 shows the partial cross-sectional view of armature windings arranged within slots of a stator icon core separated from a rotor iron core by a mechanical gap.

The region surrounded by a dotted line is focused on for numerical analyses in this study. Figure 3 shows three kinds of numerical analysis models used here. The electromagnetic fields in these models are numerically calculated based on the *H*-formulation [29–32] by using the COMSOL Multiphysics® software [33]. Figure 3(c) is called "a stator model", where a realistic situation of armature windings arranged within one of slots is considered for numerical analysis. *w* and *h* are the width and depth of iron core slot, respectively. *s* and *b* are also the width and depth of slot opening, respectively. *p* is the pitch between the slots, and δ is the gap length between the cores. *N* cables are arranged vertically and horizontally within the iron core slot, following several combinations of periodic patterns. There are six layers within the slot ($m = 6$), and the number of turns in each layer, denoted as N_1 to N_6, is 3 or 4. In the case of Fig. 3(c), the total number of turns becomes $N = 20$. The same transport current I_t is applied to each turn. The multi-strand cable is used for turn under consideration, and the single wires are used except for it. Every possible pattern of

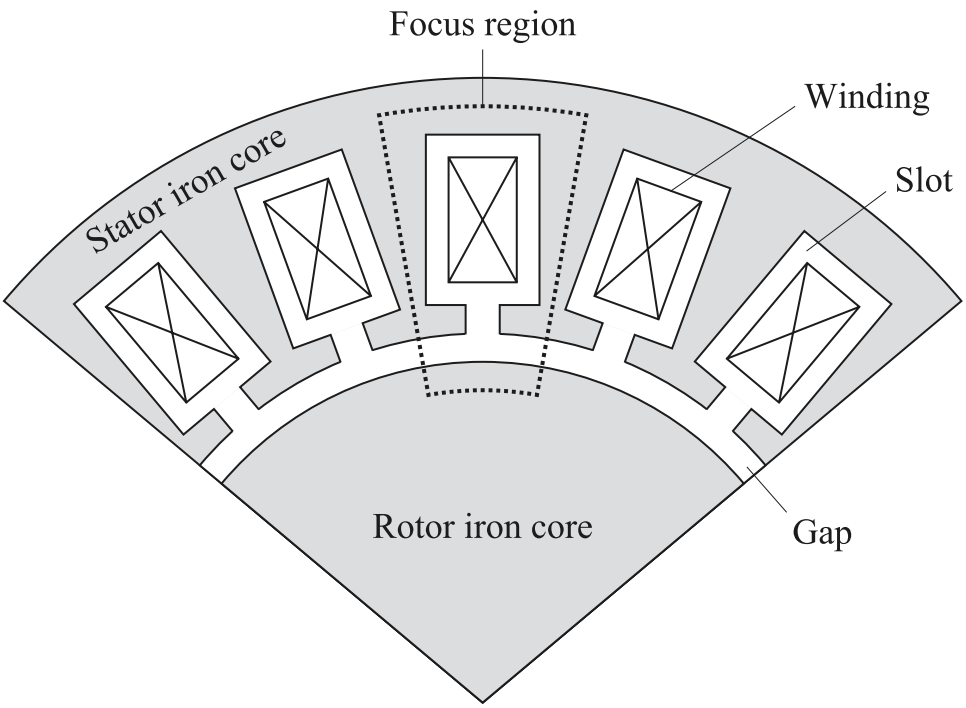

Fig. 2 Partial cross-sectional view of armature windings arranged within slots of stator icon core separated from rotor iron core by mechanical gap. The region surrounded by a dotted line is focused on for numerical analyses in this study

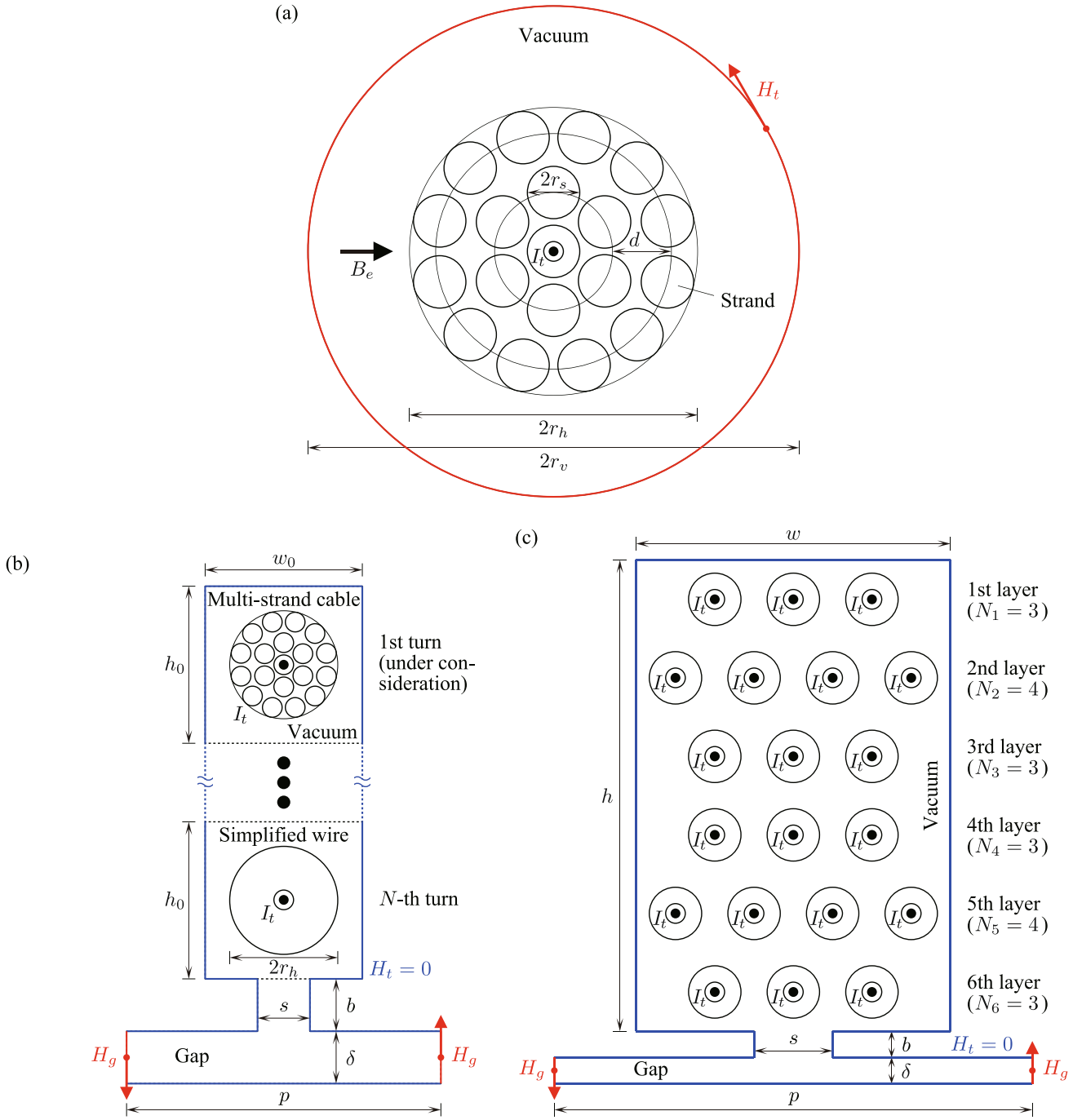

Fig. 3 Numerical analysis models called (a) lone model, (b) simple model and (c) stator model. The blue lines represent the surfaces of iron cores, where the magnetic fields become perpendicular to them if the magnetic permeability of iron core is assumed to be infinite. The Dirichlet boundary conditions are also applied on the red lines

configuration is taken into account to obtain a final result. The multi-strand cable is twisted, so that the currents in each layer of the cable become identical to each other. The boundaries indicated by blue lines represent the surfaces of iron cores, where the magnetic fields become perpendicular to them if the magnetic permeability of iron core is assumed to be infinite, and the tangential components H_t of magnetic fields are equal to zero. On the other hand, the boundaries indicated by red lines has non-zero tangential components. In the case of Fig. 3(c), the tangential magnetic fields H_g in the gap between the cores are given by $H_g = NI_t/(2\delta)$ from Ampère's law. As is customary in the H-formulation,

the vacuum region is virtually treated as a conductor with extremely high resistivity ρ_v, which is set to 1×10^{-5} Ω·m here [30]. The numerical parameters for the stator model are listed in Table 2.

Figure 3(b) is called "a simple model", which is used to understand the physical mechanism of losses in the cables within the iron core slot. A unit cell with the width w_0 and height h_0, which contains only one cable in its center, is considered first, and some of unit cells are vertically stacked to form an iron core slot. The number of unit cells, which is equal to the number N of turns within the iron core slot, is set to 1, 3 or 5. The turns are counted from the deepest point within the iron core slot as 1st to N-th turn. The cable configuration and boundary conditions similar to those in Fig. 3(c) are applied to the simple model. Figure 3(a) is called "a lone model", where a single cable is isolated in the vacuum, and the transport current I_t and an external transverse magnetic field B_e are simultaneously applied to it. The outer diameter of vacuum region, $2r_v$, is set to be ten times larger than the cable diameter $2r_h$. The boundary condition for the lone model is given by $H_t = I_t/(2\pi r_v)$. By using the lone model, the loss in each turn within the iron core slot tries to be reproduced later. The numerical parameters for the lone and simple models are listed in Table 3.

Figure 4 shows the frequency dependence of the computed losses per unit length for simple models with 1, 3 and 5 turns within the iron core slot. It is found that the numerical results of losses are constant in a small range of frequency, and the Joule losses are dominant. The Joule losses

Table 2 Numerical parameters for stator model

Number of turns arranged within slot, N	20
Number of layers within slot, m	6
Number of turns in each layer, N_i $(i = 1, \cdots, m)$	3 or 4
Slot width, w	4.8 mm
Slot depth, h	7.2 mm
Width of slot opening, s	1.2 mm
Depth of slot opening, b	0.4 mm
Pitch between slots, p	9.6 mm
Gap length between cores, δ	0.4 mm

Table 3 Numerical parameters for lone and simple models

Diameter of vacuum region in lone model, $2r_v$	8.12 mm
Resistivity of vacuum region, ρ_v	1×10^{-5} Ω·m
Number of turns arranged within slot, N	1, 3, 5
Slot width of unit cell, w_0	1.2 mm
Slot depth of unit cell, h_0	1.2 mm
Width of slot opening, s	0.4 mm
Depth of slot opening, b	0.4 mm
Pitch between slots, p	2.4 mm
Gap length between cores, δ	0.4 mm

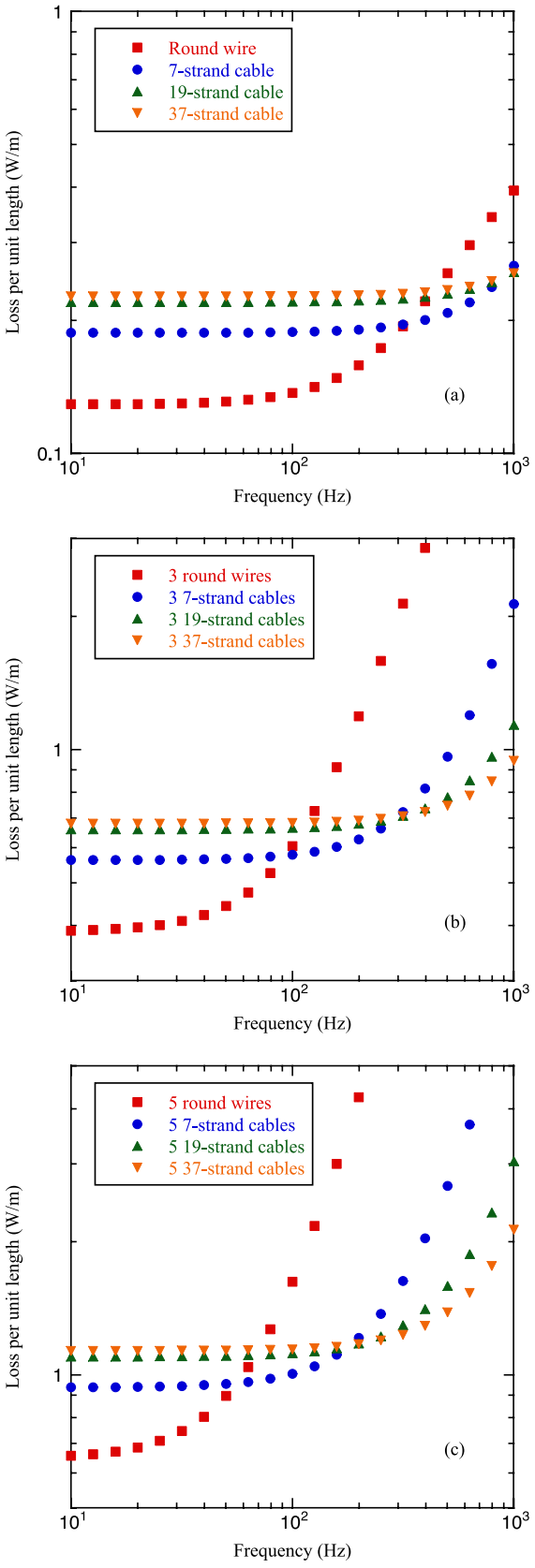

Fig. 4 Frequency dependence of numerical results of losses per unit length for simple models with (a) single turn, (b) 3 turns and (c) 5 turns within iron core slot

increase with the number of strands due to the reduction of their volume fractions. On the other hand, the numerical results of losses increase with frequency in a larger range of frequency, and the eddy-current losses become dominant. The eddy-current losses decrease with increasing the number of strands due to the reduction of their strand diameters.

Figure 5 compares the calculated losses per unit length for each turn in simple models using single round wires and cables composed of 7, 19 and 37 strands. It can be seen that the numerical results of losses in turns, counted from deepest point within the iron core slot, are identical except for turns nearest to the slot opening. For example, the losses in 1st turns of 3- and 5-turn models are same, but the loss in 1-turn model is larger than them. To give another example, the losses in 2nd turns for 3- and 5-turn models are also same, but the losses in their 3rd turns are different from each other. These loss properties can be understood on the basis of the physical mechanism illustrated in Fig. 6 [31, 34]. Figure 6(a) shows the typical profiles of magnetic lines of force within the iron core slot, where five cables are placed inside as an example. Since the permeability of iron core is assumed to be infinite, the magnetic lines of force become perpendicular to its surfaces. Figure 6(b) also shows the profiles of magnetic lines of force if the iron core were entirely

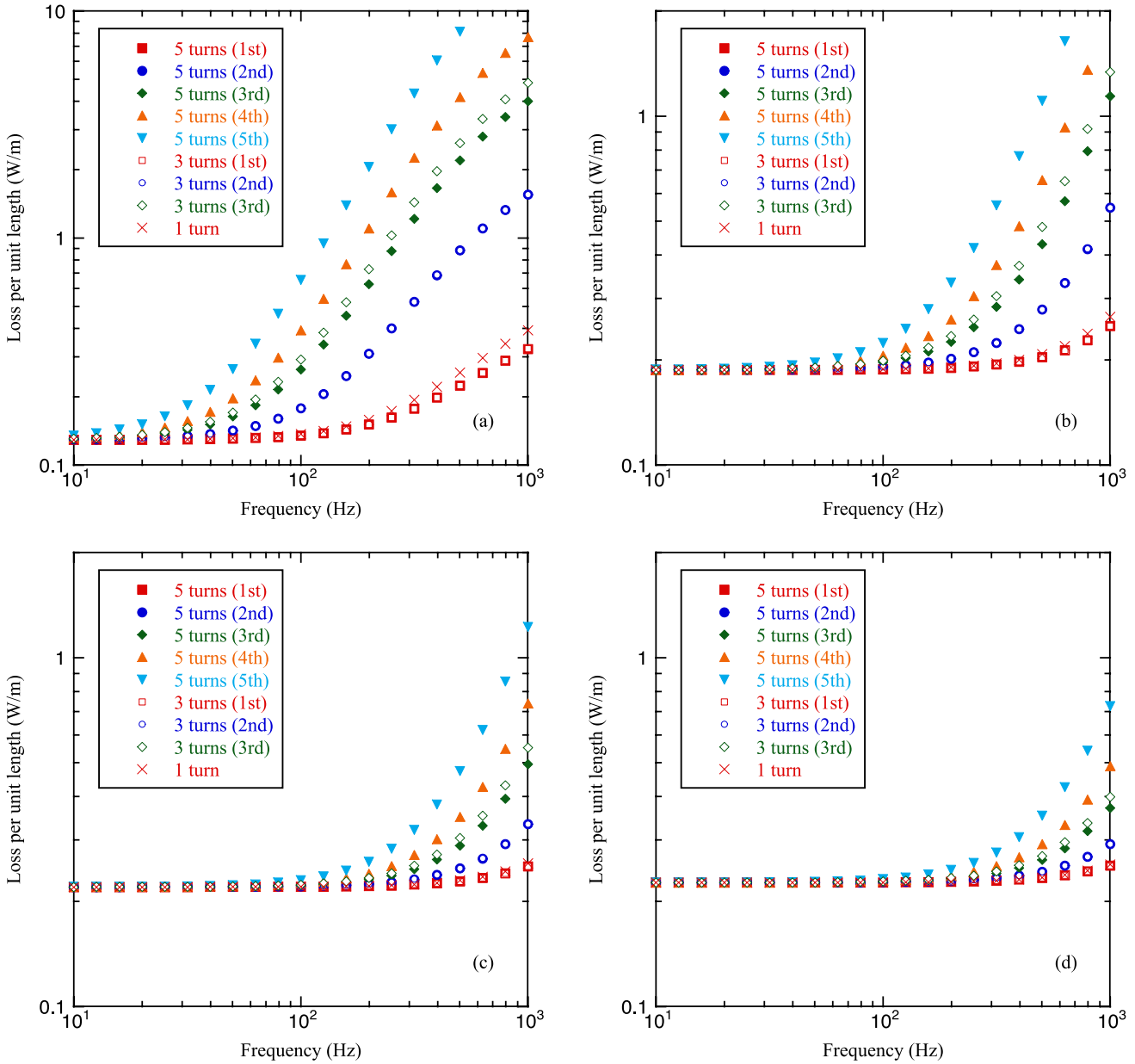

Fig. 5 Comparison between numerical results of losses per unit length for each turn in simple models with (a) single solid round wires, (b) 7-strand cables, (c) 19-strand cables and (d) 37-strand cables.

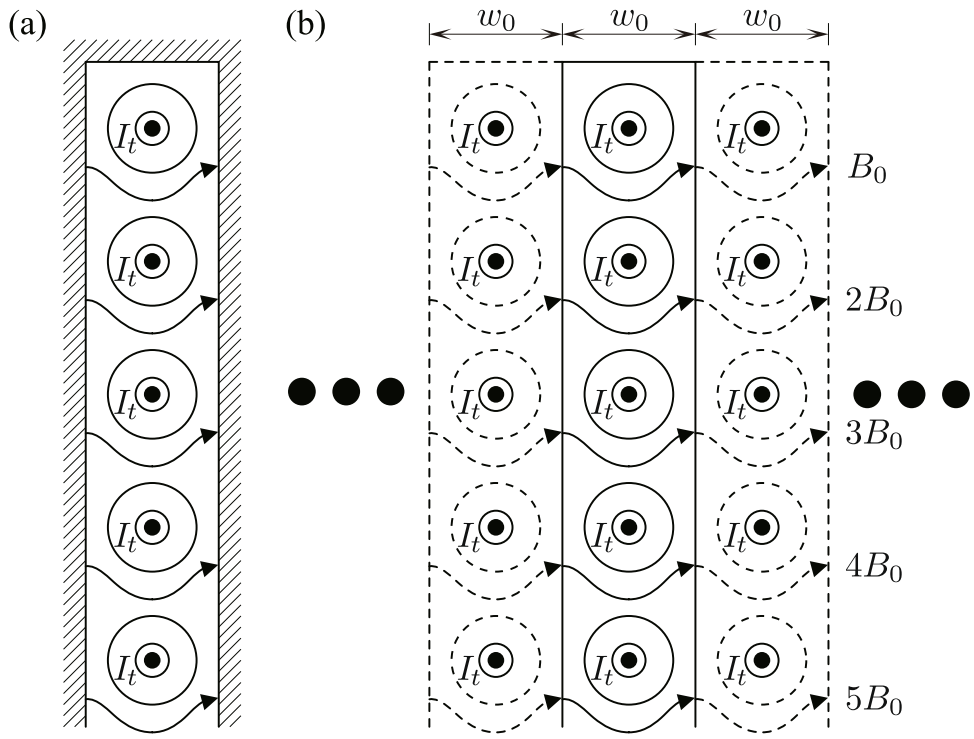

Fig. 6 Typical profiles of magnetic lines of force (a) within iron core slot and (b) for infinite arrays of mirror images

removed and the infinite number of mirror images of windings were arranged at even intervals of the slot width w_0. It can be seen that the profiles of magnetic lines of force in Fig. 6(a) have a good agreement with those in Fig. 6(b). The magnetic field B_0 generated by a single layer of horizontal array of mirror images is given by

$$B_0 = \frac{\mu_0 I_t}{w_0}, \tag{18}$$

based on an analogy with those for an infinite solenoid. In this case, the magnetic fields generated by the windings gradually increase from zero at the deepest point within the slot to NB_0 near the slot opening. In fact, however, it has to be mentioned that the reason why the losses for turns nearest to the slot opening in Fig. 5 become larger is that the magnetic fields applied to them are enhanced somewhat larger than NB_0 due to the shape effect around the slot opening.

4 Numerical and Theoretical Reproductions of Losses

In order to reproduce the numerical results of losses obtained with the simple models shown in Fig. 5 numerically, the lone models with single cables carrying the transport current I_t and simultaneously exposed to an external magnetic field $B_e = \beta B_0$ are used. Only the cases of 5 turns within the iron core slots for the simple models are focused on here. Figure 7 shows the comparison between the calculated results with the simple and lone models, plotted with closed and open symbols, respectively. The parameter β in the lone model is fixed at 0.5, 1.5, 2.5, 3.5 or 4.5. It can be seen that the numerical result of loss in each turn of the simple model below the characteristic frequency can be well reproduced by using the lone model except for turns nearest to the slot opening, to which the slightly enhanced magnetic fields are applied and whose loss becomes somewhat larger than that for the lone model.

Next, in order to reproduce the numerical results of losses for the lone models plotted with the open symbols in Fig. 7 theoretically, it is considered that the loss generated in a single cable can simply be divided into two components, the Joule loss P_J cased by only the transport current I_t and the eddy-current loss P_e caused by only the external magnetic field B_e.

Let us explain how to estimate the Joule loss P_J theoretically at first. The red symbols in Fig. 8 are obtained from the lone model with a single round wire carrying only the transport current I_t and exposed to no external magnetic field. The red curve in Fig. 8 is also drawn with the theoretical expression (17), and have a good agreement with the corresponding numerical results with the lone model. Therefore, the theoretical expression (17) for the round wire is extended to the cases of multi-strand twisted cables as follows. The multi-strand cable with N strands of $2r_s$ in diameter is regarded as a homogenized single round wire with the identical outer diameter of $2r_h$, where the subscripts s and h denote the physical quantities for strand and homogenized

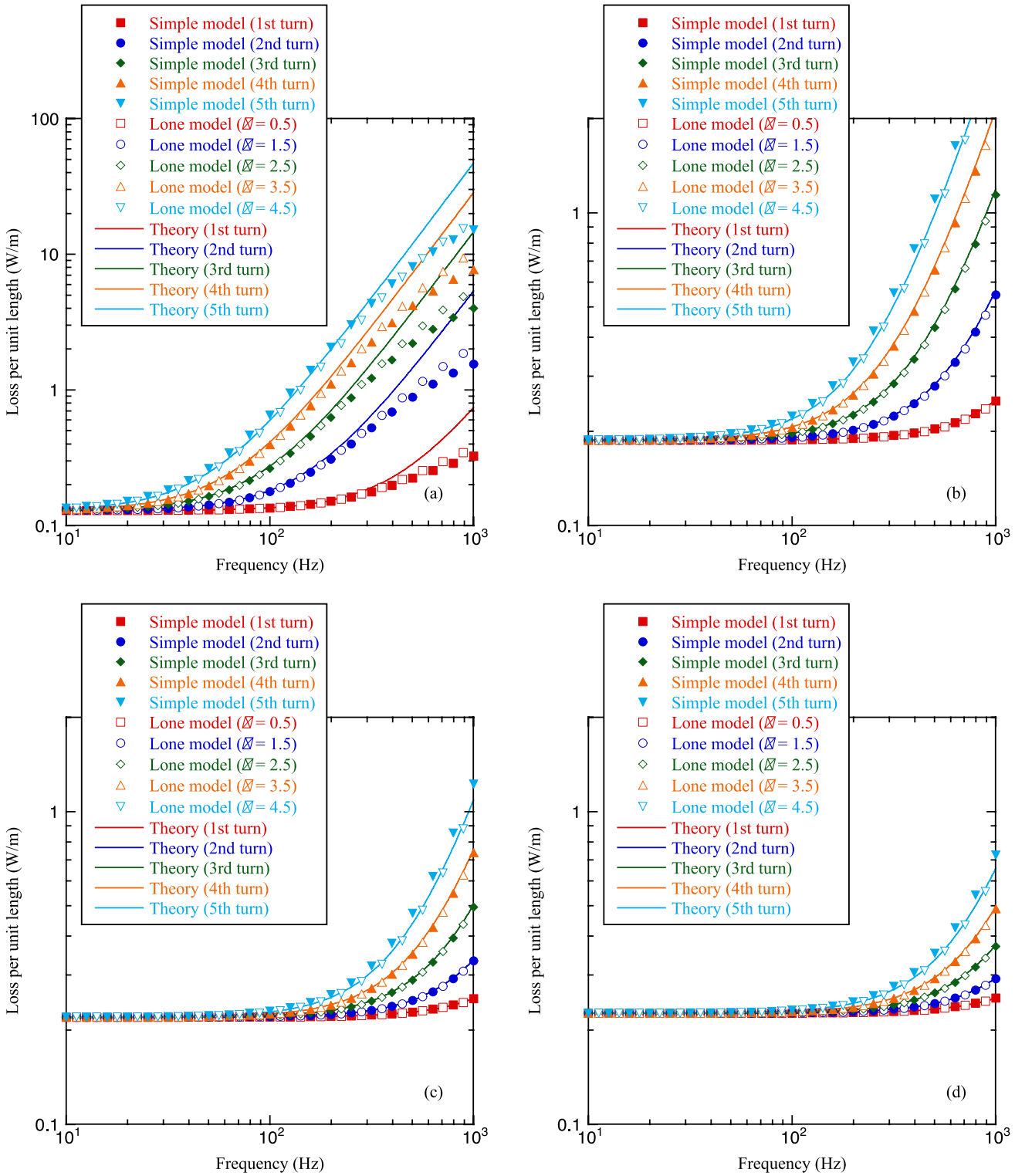

Fig. 7 Comparison among numerical results of losses per unit length for each turn in simple models, those for lone models and theoretical values with (a) single solid round wires, (b) 7-strand cables, (c) 19-strand cables and (d) 37-strand cables

wire, respectively. The similar expression (17) for the homogenized wire can be used by replacing both the resistivity ρ_s and current density J_s for the single solid round wire with $\rho_h = \rho_s/\phi$ and $J_h = \phi J_s$ for the homogenized wire, respectively. In this case, the power dissipation P_0 per unit length for low frequency can express as

$$P_0 = \rho_s J_s^2 N_s S_s = \rho_h J_h^2 S_h, \tag{19}$$

with the cross-sectional area S_h $\left(= \pi r_h^2\right)$ of the homogenized wire. Figure 8 already shows the comparison between the calculated results of losses in the lone models and the theoretical curves proposed here. It is found that the proposed theoretical procedure for estimating the Joule loss in the multi-strand cables carrying the transport current has a good agreement with the corresponding numerical results. The small discrepancy between them at very high frequency might be due to the concentration of current around the cable surface based on the skin effect.

Let us move on to theoretical estimation of the eddy-current loss P_e. The theoretical expression of eddy-current loss W_e per unit volume per cycle for an infinite slab with the thickness of $2D$ is given by [35]

$$\begin{aligned} W_e &= \frac{\pi B_m^2}{2\mu_0 \Delta} \frac{\sinh(2\Delta) - \sin(2\Delta)}{\cosh(2\Delta) + \cos(2\Delta)} \\ &\simeq \frac{2\pi B_m^2}{3\mu_0} \Delta^2, \quad \Delta \ll 1, \end{aligned} \tag{20}$$

where B_m is the amplitude of external magnetic field and $\Delta = D/\lambda_s$. If the cross-sectional area $4D^2$ of a square with the sides $2D$ is equal to that for the strand, S_s, with the diameter of $2r_s$, the theoretical expression of the eddy-current loss P_e per unit length of the multi-strand cable can be obtained as

$$P_e = N_s S_s f W_e = \frac{N_s}{6\rho_s} (\pi S_s f B_m)^2 . \tag{21}$$

It has been well known that the eddy-current loss is proportional to the second power of both the frequency f and field amplitude B_m, and inversely proportional to the resistivity ρ_s.

Figure 7 already shows the comparison between the calculated results of losses in the lone models with the single cables in vacuum and the theoretical curves drawn with solid lines. It can be seen that the numerical results of losses obtained from the lone models can be well reproduced by simple sums of theoretical values for the Joule and eddy-current losses below characteristic frequencies.

Figure 9 shows the comparison between the calculated results of losses with the stator models and the theoretical curves. The symbols represent the numerical results of total losses for all of the turns. The solid lines obtained from the proposed theoretical procedures almost agree with the numerical results. In this case, it is considered that each layer of horizontal array of cables generates a magnetic field on its lower side in Fig. 3(c) as

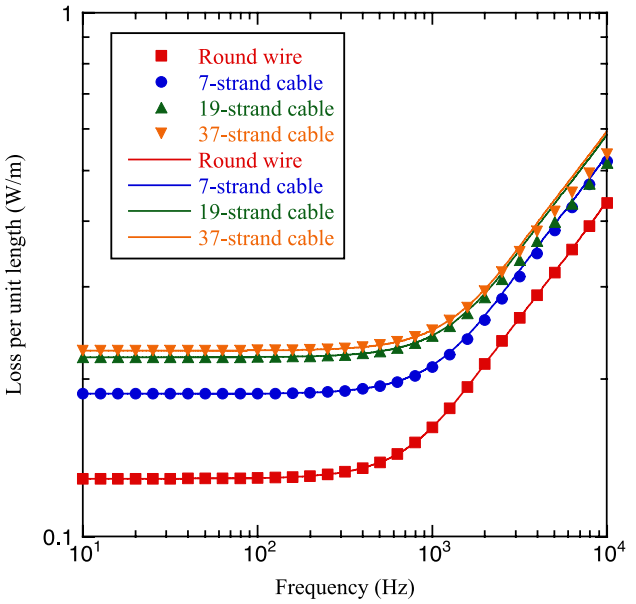

Fig. 8 Comparison between numerical results of Joule losses with lone models and theoretical values. The former are plotted with symbols, whereas the latter are drawn with solid lines

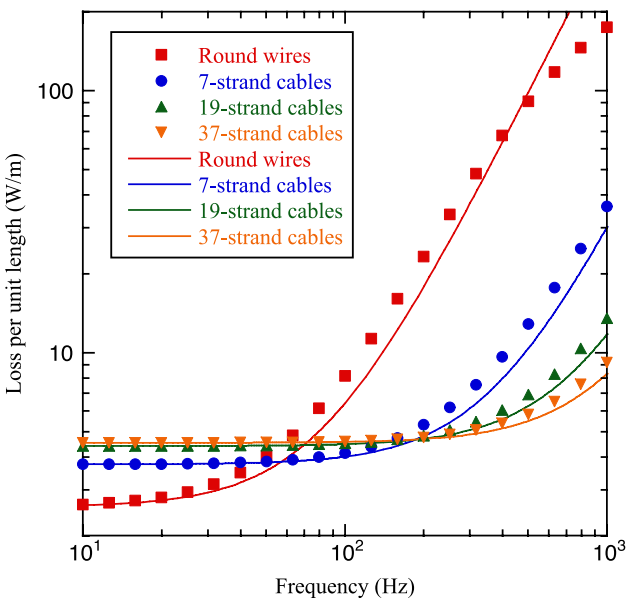

Fig. 9 Comparison between numerical results of total losses with stator models and theoretical values. The former are plotted with symbols, whereas the latter are drawn with solid lines

$$B_i = \frac{\mu_0 N_i I_t}{w}, \quad i = 1, \cdots, m, \tag{22}$$

and it is exposed to an external magnetic field of

$$B_i' = \sum_{k=1}^{i-1} B_k + \frac{B_i}{2}, \quad i = 1, \cdots, m. \tag{23}$$

The small discrepancy between the numerical results and theoretical curves at relatively high frequency is due to increases in the magnetic fields applied to the turns close to the slot opening. It is also found that the losses in the multi-strand cables at several hundred hertz are much smaller than those for the single round wires.

5 Conclusion

The armature windings of HTS motors driven by voltage from a commonly used inverter should be constructed using metallic cables to manage both unbalanced three-phase currents and frequency limitations. The losses in multi-strand metal twisted cables within one of iron core slots for armature were calculated numerically using the finite element method. The obtained results were well reproduced using both another numerical analysis model in vacuum and theoretical procedures to estimate the losses for transport current and external magnetic field. Additionally, the losses in the numerical analysis model simulating the actual armature were estimated using the finite element method, and almost agreed with theoretical predictions.

Acknowledgements This article is based on results obtained from a project, JPNP23004, subsidized by the New Energy and Industrial Technology Development Organization (NEDO).

Author Contributions All authors contributed to the study conception and design. Material preparation, data collection and analysis were performed by K.K., Y.M. and M.F. The first draft of the manuscript was written by K.K. and all authors commented on previous versions of the manuscript. All authors read and approved the final manuscript. Funding was originally planned, requested and secured by T.M., T.N., K.K. and A.K.

Funding Open Access funding provided by Sanyo-Onoda City University.

Data Availability No datasets were generated or analysed during the current study.

Declarations

Competing interests The authors declare no competing interests.

Open Access This article is licensed under a Creative Commons Attribution 4.0 International License, which permits use, sharing, adaptation, distribution and reproduction in any medium or format, as long as you give appropriate credit to the original author(s) and the source, provide a link to the Creative Commons licence, and indicate if changes were made. The images or other third party material in this article are included in the article's Creative Commons licence, unless indicated otherwise in a credit line to the material. If material is not included in the article's Creative Commons licence and your intended use is not permitted by statutory regulation or exceeds the permitted use, you will need to obtain permission directly from the copyright holder. To view a copy of this licence, visit http://creativecommons.org/licenses/by/4.0/.

References

1. Chen, J.M.: Carbon neutrality: Toward a sustainable future. The Innovation (2021). https://doi.org/10.1016/j.xinn.2021.100127
2. Vysotsky, V.S., Blagov, E.V., Kostyuk, V.V., Nosov, A.A., Fetisov, S.S., Zanegin, S.Y., Antyukhov, I.V., Firsov, V.P., Svalov, G.G., Katorgin, B.I., Rachuk, V.S.: New 30-m flexible hybrid energy transfer line with liquid hydrogen and superconducting MgB_2 cable–Development and test results. IEEE Trans. Appl. Supercond. (2015). https://doi.org/10.1109/TASC.2014.2361635
3. Hara, S., Iwami, Y., Kawasaki, R., Matsumoto, T., Shirai, Y., Shiotsu, M.: Development of liquid hydrogen cooling system for a rotor of superconducting generator. IEEE Trans. Appl. Supercond. (2021). https://doi.org/10.1109/TASC.2021.3065814
4. Makida, Y., Shintomi, T., Hamajima, T., Ota, N., Katsura, M., Ando, K., Takao, T., Tsuda, M., Miyagi, D., Tsujigami, H.: Performance of a 10-kJ SMES model cooled by liquid hydrogen thermo-siphon flow for ASPCS study. IOP Conf. Ser. Mater. Sci. Eng (2015). https://doi.org/10.1088/1757-899X/101/1/012028
5. Kamiya, K., Matsumoto, K., Numazawa, T., Masuyama, S., Takeya, H., Saito, A.T., Kumazawa, N., Futatsuka, K., Matsunaga, K., Shirai, T.: Active magnetic regenerative refrigeration using superconducting solenoid for hydrogen liquefaction. Appl. Phys. Express (2022). https://doi.org/10.35848/1882-0786/ac5723
6. Matsumoto, T., Fujita, K., Iwami, Y., Shirai, Y., Shiotsu, M., Kobayashi, H., Naruo, Y., Nonaka, S., Inatani, Y., Tanaka, H., Kodama, M., Suzuki, T.: Excitation test of solenoid MgB_2 coil under external magnetic field immersed in liquid hydrogen. IEEE Trans. Appl. Supercond. (2019). https://doi.org/10.1109/TASC.2019.2894898
7. Ohya, M., Imagawa, S., Shirai, Y., Kobayashi, H.: Energization test apparatus of HTS coils cooled by liquid hydrogen and manufacture of split-type REBCO external field coil. J. Phys: Conf. Ser. (2024). https://doi.org/10.1088/1742-6596/2776/1/012010
8. Seo, Y.-M., Noh, H.-W., Koo, T.-H., Ko, R.-K., Ha, D.-W.: Experimental study on the driving of high-temperature superconducting coil using the cryogenic heat of liquid hydrogen. Int. J. Hydrogen Energy (2025). https://doi.org/10.1016/j.ijhydene.2025.150751
9. Haberstroh, Ch., Zick, G.: A superconductive MgB_2 level sensor for liquid hydrogen. AIP Conf. Proc. (2006). https://doi.org/10.1063/1.2202474
10. Takeda, M., Matsuno, Y., Kodama, I., Kumakura, H., Kazama, C.: Application of MgB_2 wire to liquid hydrogen level sensor–External-heating-type MgB_2 level sensor. IEEE Trans. Appl. Supercond. (2009). https://doi.org/10.1109/TASC.2009.2019033
11. Kajikawa, K., Inoue, T., Watanabe, K., Kanazawa, M., Yamada, Y., Kobayashi, H., Taguchi, H., Aoki, I.: Proposal of a new type of superconducting level sensor for liquid hydrogen with MgB_2 wires. Phys. Procedia (2012). https://doi.org/10.1016/j.phpro.2012.06.311
12. Kajikawa, K., Kuga, H., Inoue, T., Watanabe, K., Uchida, Y., Nakamura, T., Kobayashi, H., Hongo, M., Kojima, T., Taguchi, H., Naruo, Y., Wakuda, T., Tanaka, K.: Development of a liquid hydrogen transfer pump system with MgB_2 wires. Cryogenics (2012). https://doi.org/10.1016/j.cryogenics.2012.08.007
13. Kajikawa, K., Kuga, H., Inoue, T., Watanabe, K., Uchida, Y., Nakamura, T., Wakuda, T., Tanaka, K.: Demonstration of transfer of liquid helium using a pump system with MgB_2 wires. J. Supercond. Nov. Magn. (2013). https://doi.org/10.1007/s10948-012-1926-1
14. Kajikawa, K., Uchida, Y., Nakamura, T., Kobayashi, H., Wakuda, T., Tanaka, K.: Development of stator windings for fully superconducting motor with MgB_2 wires. IEEE Trans. Appl. Supercond. (2013). https://doi.org/10.1109/TASC.2013.2240033
15. Lee, J.K., Park, S.H., Kim, Y., Lee, S., Joo, H.G., Kim, W.S., Choi, K., Hahn, S.Y.: Test results of a 5 kW fully superconducting

homopolar motor. Prog. Supercond. Cryo (2013). https://doi.org/10.9714/psac.2013.15.1.035
16. Huang, Z., Zhang, M., Wang, W., Coombs, T.A.: Trial test of a bulk-type fully HTS synchronous motor. IEEE Trans. Appl. Supercond. (2014). https://doi.org/10.1109/TASC.2013.2296142
17. Nakamura, T., Yoshikawa, M., Ikeda, K., Karashima, T., Ogasa, T., Nishino, R., Itoh, Y., Terazawa, T., Furuse, M., Fukui, S.: Load test and variable speed control of a 50-kW-class fully superconducting induction/synchronous motor for transportation equipment. IEEE Trans. Appl. Supercond. (2019). https://doi.org/10.1109/TASC.2019.2902504
18. Miyazaki, H., Iwakuma, M., Emori, Y., Sasa, H., Yoshida, K., Sato, S., Miura, S., Sagara, I., Suzuki, Y., Konno, M., Hirai, H., Izumi, T.: Fabrication and test of a 400 kW-class fully superconducting synchronous motor using REBCO tape for an electric propulsion system. IEEE Trans. Appl. Supercond. (2024). https://doi.org/10.1109/TASC.2023.3345291
19. Nakamura, T., Yamamoto, M.: A study on optimal winding configuration for high-temperature superconducting induction/synchronous motors. 70th Spring Meeting of Jpn. Soc. Appl. Phys., 17p-D215-10 (2023)
20. Sumption, M.D., Murphy, J., Susner, M., Haugan, T.: Performance metrics of electrical conductors for aerospace cryogenic motors, generators, and transmission cables. Cryogenics (2020). https://doi.org/10.1016/j.cryogenics.2020.103171
21. Manolopoulos, C.D., Iacchetti, M.F., Smith, A.C., Miller, P., Husband, M.: Litz wire loss performance and optimization for cryogenic windings. IET Electr. Power Appl. (2023). https://doi.org/10.1049/elp2.12279
22. Kalsi, S.S., Storey, J.G., Lumsden, G., Badcock, R.A.: Airplane motors employing superconducting DC field windings and conventional conductor AC windings. IOP Conf. Ser. Mater. Sci. Eng (2024). https://doi.org/10.1088/1757-899X/1302/1/012017
23. Kwon, J., Sumption, M.D., Collings, E.W., Kovacs, C., Haugan, T., Peng, X., Rindfleisch, M.: AC loss comparisons of various conductors for cryogenic propulsion motor windings of electric aircraft. Proc. of AIAA Aviation Forum & Ascend 2024 (2024). https://doi.org/10.2514/6.2024-3961
24. Wang, Y., Zhou, L., Yuan, Q., Song, X.: Feasibility study of high temperature superconducting machines for electric aircraft. Proc. of 2024 IEEE 7th Int. Electrical & Energy Conf (2024). https://doi.org/10.1109/CIEEC60922.2024.10583838
25. Chow, C.C.T., Zhang, M., Chau, K.T.: Analytical AC loss comparison between REBCO, MgB_2, copper, and aluminum Litz wires for cryogenic electrical machines. IEEE Trans. Appl. Supercond. (2025). https://doi.org/10.1109/TASC.2024.3519419
26. Moriguchi, S., Udagawa, K., Hitotsumatsu, S.: Iwanami Mathematical Formula III Special Functions. pp. 170–174, 186–188. Iwanami Shoten, Tokyo (1995)
27. Engineering, E.: CryoComp **5**, 1 (2011)
28. Iwasa, Y.: Case Studies in Superconducting Magnets (1st ed.). p. 393. Plenum Press, New York (1994)
29. Kajikawa, K., Hayashi, T., Yoshida, R., Iwakuma, M., Funaki, K.: Numerical evaluation of AC losses in HTS wires with 2D FEM formulated by self magnetic field. IEEE Trans. Appl. Supercond. (2003). https://doi.org/10.1109/TASC.2003.812415
30. Kajikawa, K., Hayashi, T., Yoshida, R., Iwakuma, M., Funaki, K.: Influence of vacuum region on AC losses in superconducting wires with 2D FEM formulated by self-magnetic field. Physica C (2003). https://doi.org/10.1016/S0921-4534(03)01116-X
31. Kajikawa, K., Osaka, R., Nakamura, T., Sugano, M., Wakuda, T.: AC loss evaluation of MgB_2 superconducting windings located in a stator core slot with a finite-element method. J. Supercon. Nov. Magn (2011). https://doi.org/10.1007/s10948-010-0870-1
32. Shen, B., Grilli, F., Coombs, T.: Review of the AC loss computation for HTS using H formulation. Supercond. Sci. Technol. (2020). https://doi.org/10.1088/1361-6668/ab66e8
33. COMSOL: COMSOL Multiphysics 6.2 (2023)
34. Kajikawa, K., Yanagisawa, S., Nakamura, T.: AC loss evaluation of superconductor strips located inside iron core slots. IEEE Trans. Appl. Supercond. (2024). https://doi.org/10.1109/TASC.2023.3341920
35. Funaki, K., Sumiyoshi, F.: Multifilamentary Wires and Conductors. pp. 125–129. Sangyo Tosho, Tokyo (1995)

Publisher's Note Springer Nature remains neutral with regard to jurisdictional claims in published maps and institutional affiliations.